Submitted to ADVANCED ENERGY MATERIALS

DOI: 10.1002/aenm.((please add manuscript number))
Article type: Full paper

Morphology and Efficiency: The case of polymer/ZnO solar cells

L. Jan Anton Koster, Ole Stenzel, Stefan D. Oosterhout, Martijn M. Wienk, Volker Schmidt, and René A. J. Janssen*

[*]Dr. L. J. A. Koster
Molecular Electronics, Zernike Institute for Advanced Materials, Nijenborgh 4, 9747 AG Groningen, The Netherlands
Email: l.j.a.koster@rug.nl

O. Stenzel and Prof. Dr. V. Schmidt
Institute for Stochastics, Ulm University, 89069 Ulm, Germany

Dr. S. D. Oosterhout
Molecular Materials and Nanosystems, Eindhoven University of Technology, PO Box 513, 5600 MB Eindhoven, the Netherlands
Present address
National Renewable Energy Laboratory
15013 Denver West Pkwy
Golden, CO 80401-0031
United States

Dr. M. M. Wienk, and Prof. Dr. R. A. J. Janssen
Molecular Materials and Nanosystems, Eindhoven University of Technology, PO Box 513, 5600 MB Eindhoven, the Netherlands

Keywords: conjugated polymers; organic electronics; photovoltaic devices; solar cells; zinc oxide

ABSTRACT

The performance of polymer solar cells critically depends on the morphology of the interface between the donor- and acceptor materials that are used to create and transport charge carriers. Solar cells based on poly(3-hexylthiophene) and ZnO were fully characterized in terms of their efficiency and three-dimensional (3D) morphology on the nanoscale. Here, we establish a quantitative link between efficiency and morphology by using the experimental 3D morphology as direct input for a 3D optoelectronic device model. This model includes the effects of exciton diffusion and quenching; space-charge; recombination, generation, drift and diffusion of charge carriers; and the injection/extraction of carriers at the contacts. The observed trend in internal quantum efficiency as a function of layer thickness is reproduced with a single set of parameters. Several morphological aspects that determine the internal quantum efficiency are discussed and compared to other organic solar cells. This first direct use of morphological data in an optoelectronic device model highlights the importance of morphology in solar cells.

1. Introduction

Organic solar cells have the potential to become a major source of renewable energy in the next several years. Progress in efficiencies has been impressive,[1-4] with values of around 10% being reported by several groups and companies. To create charges, two different materials with offset energy levels are used. At the resulting heterojunction between the donor and acceptor materials excitons can be split up into charge carriers. As the exciton diffusion length in organic materials is typically much smaller than the thickness needed to absorb a sizable fraction of the incident light (typically 100-200 nm), a bulk heterojunction (BHJ) architecture is employed to ensure that excitons are generated close to a donor/acceptor interface. Thus, the generation of charges is favored by a finely intermixed morphology. Transporting those charges to the electrodes, however, is more efficient if the BHJ is a coarse one. These competing demands on morphology make it a key factor in solar cell optimization. Hybrid solar cells based on an organic donor and an inorganic acceptor material offer the possibility of combining the high carrier mobilities of inorganic materials with the ease of processing and tunability of conjugated polymers.[5-10] Besides yielding efficient devices, the high density of ZnO makes it possible to use electron microscopy and tomography to obtain detailed information on the donor/acceptor morphology. The interpretation of these techniques is simplified by the fact that no 'mixed phase' of donor and acceptor is present. This makes the assignment of donor or acceptor material (binarization) to a part of the layer straightforward.

In a previous publication we reported the fabrication of poly(3-hexylthiophene)/ZnO BHJ solar cells.[11] Briefly, poly(3-hexylthiophene) (P3HT) and diethylzinc were dissolved in a mixture of chlorobenzene, toluene, and tetrahydrofuran. This solution was spin-cast onto glass substrates with a transparent electrode. During spin-casting, the diethylzinc reacts with moisture from the ambient causing hydrolysis and the formation of zinc hydroxide.

Subsequent annealing at 100 ºC yields condensation of the hydroxide to form an interpenetrating network of ZnO in a P3HT matrix. The presence of crystalline P3HT and ZnO domains was evidenced by electron diffraction experiments. The thickness of the P3HT/ZnO layer was varied by using different spin-casting velocities while keeping the P3HT and diethylzinc concentrations constant. The devices were completed by the deposition of an aluminum electrode. A 1:1 (by weight) ratio of P3HT to ZnO (assuming full conversion of the diethylzinc) proved to yield the highest power conversion efficiency of 2%. This ratio translates into a ZnO content of 20% by volume, which is considerably smaller than what is typical in polymer/fullerene solar cells. Due to evaporation of diethylzinc during spin-casting the actual ZnO content is even smaller for devices spun at high speeds.

Figure 1 shows the internal quantum efficiency (IQE), which was calculated as the ratio between the measured short-circuit current and the number of absorbed AM1.5 photons per unit area and time.[11] Interestingly, devices thinner than approximately 120 nm have an IQE that is smaller than thicker ones, despite the fact that in thick films charge carriers have to travel further to the electrodes. Photo-induced absorption measurements indicate that exciton quenching in thin P3HT/ZnO layers is not quantitative, while thicker layers generate charges more efficiently.[11]

The morphology of three representative photoactive layers of different thicknesses (57 nm, 100 nm and 167 nm) was imaged with 3D electron tomography.[11, 12] Due to experimental constraints only about 60% of the layer thickness could be used for binarization. In order to obtain the full thickness, the additional volume was added by mirroring the original data (see Supporting Information). The reconstructed volumes are shown in **Figure 2**. Clearly, the morphology is very different for the three thicknesses studied. The thinnest sample shows very large P3HT domains, which is one of the reasons for the low IQE of thin layers. Previously, we studied the effects of morphology on exciton quenching and found that exciton decay in the P3HT phase is a significant loss in the thin layers. Here we seek to significantly

extend this analysis by including the effect of charge transport on IQE. Recently, we have developed a model that can generate realistic morphologies (with arbitrary layer thicknesses) from spatial stochastic modeling to facilitate further optoelectronic device modeling studies.[13]

2. Device model

In order to quantitatively link the morphology of the photoactive layers, as shown in Figure 2, to the IQE (see Figure 1) we have developed a 3D optoelectronic device model. It is clear that given the complex 3D nature of the morphologies a full 3D treatment is required. The optical part of this model includes exciton diffusion and decay within the polymer phase and exciton quenching at interfaces. After free charge carriers have been formed at the P3HT/ZnO interface, the electrical part of the model describes their subsequent transport to the electrodes, their effect on the electric field and possible bimolecular recombination across the P3HT/ZnO interface. Additionally, the injection of charge carriers by the contacts (dark current) is included. The morphologies as depicted in Figure 2 define which parts of the simulation volume correspond to either donor or acceptor material and serve as direct input for the simulations. The interface is defined midway between a donor and an acceptor grid point. Cyclic boundary conditions are applied in the lateral directions.

We base our simulation on a drift-diffusion approach rather than a Monte Carlo model as drift-diffusion is significantly faster.[14] This enables us to run simulations on the large volumes that these morphologies require (up to 6.2 million grid points), vary parameters, and calculate full current-voltage characteristics, all under normal operating conditions. As is customary in current Monte Carlo models for organic solar cells,[15-17] any holes (electrons) in the acceptor (donor) phase are neglected. A comparison between Monte Carlo data from the literature and this model will be presented in the next section.

2.1. Model details

The local exciton density X, within the P3HT phase is calculated by solving the exciton diffusion equation,

$$0 = -\frac{X}{\tau} + D_X \nabla^2 X + g, \quad (1)$$

where τ is the exciton lifetime, D_X is the exciton diffusion constant, and g is the volume generation rate of excitons. For simplicity, g is taken uniform across the layer. Kotlarski *et al.* have shown this approximation is a good one for polymer/fullerene layers thinner than 250 nm.[18] Exciton quenching by charge transfer at the P3HT/ZnO interface is implemented by requiring the exciton density in the ZnO be zero. It is assumed that charge transfer to ZnO directly yields free charge carriers.[19] Exciton quenching at the electrodes due to energy transfer is taken into account by setting the exciton density equal to zero at the electrodes. We know from previous work that exciton quenching at the electrodes can be significant for thin P3HT/ZnO layers.[11]

At the P3HT/ZnO interface, charge carriers are generated and may also recombine. Once the exciton density X is known, the generation rate G of free carriers at the interface can be calculated. Let subscript D (A) denote the donor (acceptor) phase. Then the generation rate of free carriers at either side of the heterojunction is given by

$$G_A = G_D = D_X \frac{X_D}{(\delta x)^2}, \quad (2)$$

where δx is the grid spacing. Bimolecular recombination of carriers across the interface is given by

$$R_A = R_D = \gamma n_A p_D, \quad (3)$$

where n_A and p_D are the electron and hole density, respectively.

The recombination rate constant γ is given by the Langevin expression[20]

$$\gamma = \gamma_{\text{pre}} \frac{q}{\varepsilon}(\mu_n + \mu_p), \quad (4)$$

where q is the elementary charge and ε is the dielectric constant. Equation (4) is modified to include a reduction factor γ_{pre}. The electron (hole) mobility in the acceptor (donor) phase is denoted by μ_n (μ_p). Equation (4) implies that the grid spacing corresponds to a physical length, equivalent to the hopping distance. The current flow away from the interface in any given direction is related to the net generation (i.e. generation minus recombination) rate of carriers in that direction.

Away from the P3HT/ZnO interface, i.e. in the bulk of the donor/acceptor domains, carrier flow is governed by drift and diffusion; for electrons

$$J_n = -qn\mu_n \nabla V + qD_n \nabla n \tag{5}$$

and for holes

$$J_p = -qp\mu_p \nabla V - qD_p \nabla p. \tag{6}$$

It is assumed that the Einstein relation between mobility and diffusivity $D_{n,p}$ holds.[21,22] The potential is solved from the Poisson equation;

$$\nabla^2 V = \frac{q}{\varepsilon}(n - p). \tag{7}$$

The boundary condition on the potential is given by

$$q\left(V_L - V_0 + V_{\text{applied}}\right) = W_{\text{anode}} - W_{\text{cathode}}, \tag{8}$$

where V_L and V_0 are the potentials at either electrode, V_{applied} is the applied voltage, and W_{anode} and W_{cathode} are the anode, respectively cathode work functions.

The boundary condition on the electron (hole) density at the electrodes is given by

$$n(p) = N_{cv} \exp\left(-\frac{\varphi_{A(D)}}{V_t}\right), \tag{9}$$

where $\varphi_{A(D)}$ is the barrier between the LUMO (HOMO) of the acceptor (donor) and the electrode and N_{cv} is the effective density of states. After Eq. (1) has been solved to yield the exciton density, the system of Eqs. (2)-(9) is solved iteratively using Gummel iteration.[23] The post-processing is done using the Mayavi Data Visualizer.[24]

3. Results and discussion

3.1. Comparison with Monte Carlo simulations

Theoretical three-dimensional morphologies have been included in Monte Carlo studies.[15,16,25] Monte Carlo models monitor all individual charge carriers and their interactions, making them very computationally costly. Because of this, Monte Carlo studies on organic solar cells often focus on sub-processes rather than on a complete device,[26-29] use theoretical rather than experimental morphologies, and direct comparison with experimental current-voltage data has proved elusive. Monte Carlo simulations do include more microscopic detail as they track individual charge carriers. This makes it possible to include, for example, short-range Coulomb interactions and energetic disorder. The drift-diffusion approach focuses on carrier density distributions rather than on individual carriers, sacrificing microscopic detail for much reduced computational cost. As a result, it is not a priori clear whether the drift-diffusion approach is still appropriate given the small and complex morphological features that characterize organic BHJ solar cells. We therefore compare the results of drift-diffusion simulations with Monte-Carlo data from the literature.[16]

Kimber *et al.* have published a Monte-Carlo study on the effect of different morphologies.[16] One of the morphology classes they have considered was obtained by so-called simulated annealing (SA).[30] This technique involves randomly choosing a pair of neighboring sites (voxels) and probabilistically admitting a swap based on the total energy. To encourage phase separation, the interfacial energies of the constituent phases are chosen such that a configuration with a smaller interfacial area is lower in energy. At a given volume ratio the morphology is solely characterized by the average feature size b. At a 1:1 volume ratio of donor-to-acceptor $b = 3V/A$, where V is the total volume and A is the interfacial area. Kimber *et al.* demonstrated that the fraction of carriers that recombine bimolecularly increases for finer morphologies, i.e. for smaller b. **Figure 3** (inset) shows their data for bimolecular recombination loss ζ_{BR} in the range of feature sizes that is relevant for the P3HT/ZnO

morphologies studied in this paper. These P3HT/ZnO morphologies have feature sizes *b* ranging from 5.5 nm (167 nm) to 7.5 nm (57 nm).

For the drift-diffusion simulations we take our parameters, as far as possible, from the paper by Kimber *et al.*, see Table 1, while bimolecular recombination was assumed to be of the (unmodified, $\gamma_{pre} = 1$) Langevin type. However, not all parameters can be retrieved and there remain differences between the physics that the models describe. This precludes a direct quantitative comparison. A qualitative comparison, however, is possible as the trend of ζ_{BR} as a function of feature size is not very sensitive to these details. The obtained bimolecular recombination loss ζ_{BR} is very similar to the Monte-Carlo data, see Figure 3. Given how different these methodologies are, the agreement between the Monte-Carlo and drift-diffusion results is satisfactory. In a recent paper, Stenzel *et al.* compared the structural and physical characteristics of SA morphologies with those of P3HT/ZnO.[13] They have found that these morphologies are structurally very different, for example SA morphologies are isotropic, P3HT/ZnO morphologies are not. However, we believe this favorable comparison to be a good test of the suitability of 3D drift-diffusion models for simulating complex BHJ devices.

3.2. Modeling P3HT/ZnO solar cells

We now turn to the P3HT/ZnO data and seek to explain the IQE (see Figure 1) for the three different morphologies. There exist several different values for the exciton diffusion length in P3HT in the literature ranging from 2.6 nm to 8.5 nm.[31-34] We assume the exciton diffusion length[35] to be equal to 5 nm as this appears to be a reasonable value. In a 50-nm thick P3HT/ZnO blend, the hole mobility in the P3HT phase was found to be 4×10^{-8} m^2/Vs,[36] which is comparable to the mobility in pristine P3HT.[37] The mobility in the ZnO phase proved difficult to measure. However, as there are no signs of space-charge buildup in these solar cells it is reasonable to assume that the electron- and hole mobility must be similar.[38] We note that a slightly lower (2.8×10^{-9} m^2/Vs) electron mobility was reported for a poly(*p*-

phenylene vinylene) (PPV) derivative blended with ZnO nanoparticles (25 vol.-%).[19] As inter-particle transport might be problematic it is not surprising that the mobility in the nanoparticle blend is lower.

In fitting to the IQE data a single set of parameters was used (see Table 2): Only the morphologies, their corresponding thicknesses and the number of absorbed photons as determined from the experiments were changed between simulations. Bimolecular recombination in P3HT/fullerene blends is significantly reduced relative to the Langevin rate (corresponding to $\gamma_{pre} << 1$),[39] especially under conditions where the domain size of the phase separation has increased. PPV/fullerene blends do not show this reduction,[39] and the reduction of Langevin recombination appears to be a property associated with phase-separated P3HT. We use the Langevin reduction factor γ_{pre} as a free parameter in our simulations. The resulting IQE data are shown in Figure 1, obtained with $\gamma_{pre} = 0.03$. Clearly, the IQE can be reproduced with our model.

The structural differences between the morphologies lessen as thicker layers are considered.[13] In other words, beyond approximately 150-200 nm thickness, the morphologies are fairly similar. This allows us to further test our modeling approach. By using the mirror procedure as outlined above, a morphology of 220 nm thickness was emulated by adding extra thickness to the 167-nm thick morphology. As this should yield a reasonably good approximation of the real morphology at 220 nm thickness, the calculated IQE should be close to the experimental value (40-45%). The resulting IQE (43%, see Figure 1) indeed agrees with the experimental data, which demonstrates the predictive power of the optoelectronic model.

Figure 4 (a) shows the simulated current-voltage characteristics for the 57, 100, and 167-nm morphologies together with the experimental current-voltage characteristics of a 162-nm thick device. The similarity between simulation and experiment is striking. This reaffirms the suitability of our modeling approach. We note however, that the experimental current-

voltage characteristics display some scatter, due to the sensitivity of the performance to subtleties in the fabrication conditions, especially related to the ambient humidity and solvent evaporation rate. This scatter complicates fitting directly to the current-voltage characteristics of individual devices. Although some scatter is also borne out in the IQE (as shown in Figure 1) it is less pronounced. Therefore, we chose to focus on reproducing the trend in IQE.

To further analyze the differences in IQE that the different layers display, we plot the exciton loss ζ_X and the bimolecular recombination loss ζ_{BR} in Figure 4(b). Clearly, the thicker layers have better exciton harvesting (lower ζ_X) but more charge carriers recombine (higher ζ_{BR}). The overall IQE is a tradeoff between these two quantities: The 57-nm morphology with its coarse phase separation is very good at transporting charges to the electrodes, but has limited exciton harvesting capability. On the other hand, the 167-nm thick morphology has significant recombination losses.

It should be noted that the recombination of carriers is not homogeneously distributed throughout the device. **Figure 5** shows the recombination rate averaged in the plane parallel to the substrate for the 167-nm morphology. At short-circuit the recombination rate is low except near the anode. This is a consequence of the large hole density that is present at the anode. Electrons in the ZnO phase are prone to recombine with these carriers. There are, however, hotspots of recombination, such as isolated ZnO clusters and cul-de-sacs in the morphology. These “morphological traps” cause the recombination rate to fluctuate in across the layer. As the bias voltage is increased, more and more carriers are injected from the contacts and the recombination rate increases. At open-circuit all charge carriers recombine and generation and bimolecular recombination cancel.[40] As a consequence, the recombination rate is fairly uniform throughout the layer.

3.3 Influence of morphological features

From Figure 2 it is clear that not all ZnO is connected to the cathode as there are some isolated islands of ZnO that are completely surrounded by P3HT. Electrons generated in these isolated clusters cannot flow out of the device and eventually recombine with holes in the P3HT phase. Additionally, electrons generated in some connected parts of the ZnO phase have to travel against the built-in field (*i.e.* towards the anode) for part of their journey before reaching the cathode. Carriers generated in these cul-de-sacs may not be able to reach the cathode. To assess the influence of both morphological features we consider the 167-nm morphology as they are most prominent at this thickness.[11] In this morphology, 92% of ZnO is connected to the cathode, but only 80% is connected via a strictly rising path. The distribution of isolated clusters is not uniform: fewer of these clusters are found far away from the main ZnO structures.[41] After removing the isolated ZnO clusters, fewer excitons are quenched by ZnO yet the IQE remains constant (see Table 3). This indicates that the influence of this type of defect is negligible. As **Figure 6** illustrates, isolated ZnO clusters only interfere with the main ZnO phase connected to the electrode (the "backbone") if they are close enough to "steal" some of its excitons: if the cluster is close to the ZnO backbone, then the current is decreased as fewer excitons are harvested by the backbone. On the other hand, if the cluster is far away from the ZnO backbone, neither the exciton harvesting is effected nor is the current. The effect on the electric field is small as the electrons on the ZnO cluster are shielded by the holes at the other side of the interface.

Removing the cul-de-sacs is accomplished by removing (*i.e.* changing the grid point from ZnO to P3HT) all grid points that are not monotonously connected to the cathode. Note, that this also includes any isolated ZnO clusters. Surprisingly, the IQE of the 167-nm morphology is somewhat lower after removing the cul-de-sacs: The resulting exciton quenching is reduced, resulting in fewer free charge carriers, but on the other hand bimolecular recombination is also reduced. The tradeoff between exciton quenching and

bimolecular recombination depends on the depth of the cul-de-sacs, charge carrier mobility, electric field, etc. and will depend on the exact details of the system under study. Figure 6 (d)-(f) illustrates an example where removing the cul-de-sacs does improve the IQE.

The discussion of isolated clusters and cul-de-sacs in the morphology can also be relevant to other BHJ systems, *e.g.* polymer/fullerene or small molecule/fullerene solar cells. In systems where donor and acceptors form distinct phases, morphological traps can and enhance recombination losses.[42]

4. Conclusion

In sum, we have studied the relation between morphology and performance of BHJ solar cells in unprecedented detail: Solar cells based on P3HT and ZnO were fully characterized in terms of their efficiency and three-dimensional (3D) morphology on the nanoscale. We have established a quantitative link between efficiency and morphology by using the experimental 3D morphology as direct input for a 3D optoelectronic device model. This model includes the effects of exciton diffusion and quenching; space-charge; recombination, generation, drift and diffusion of charge carriers; and the injection/extraction of carriers at the contacts. By comparing the model with Monte-Carlo data from the literature we confirmed that a drift-diffusion approach is still viable at these length-scales. The observed trend in internal quantum efficiency as a function of layer thickness can be reproduced with a single set of parameters. The IQE is a tradeoff between exciton harvesting and charge transport: The 57-nm morphology with its coarse phase separation is very good at transporting charges to the electrodes, but has limited exciton harvesting capability. On the other hand, the 167-nm thick morphology has significant recombination losses. Isolated clusters of acceptor material that are more than a few times the exciton diffusion length away from the main acceptor backbone do not affect the overall device efficiency. The impact of cul-de-sacs, however, is more complex and depends on the local electric field, the depth of the cul-de-sac, etc. For this

particular set of morphologies, efforts to remove isolated clusters of ZnO or cul-de-sacs in the ZnO phase will not improve device performance. This first direct use of morphological data in an optoelectronic device model shows that it is indeed possible to quantitatively link morphology to device performance.

Supporting Information
Supporting Information is available online from the Wiley Online Library or from the author.

Acknowledgements
L.J.A.K. acknowledges support by a grant from STW/NWO (VENI 11166) and thanks A. B. Walker (University of Bath) for detailed information regarding the Monte-Carlo data in Ref. 15. O.S. and V.S. acknowledge financial support by the German Research Society (DFG) under the Priority Programme: 'Elementary Processes of Organic Photovoltaics' (SPP 1355).

Received: ((will be filled in by the editorial staff))
Revised: ((will be filled in by the editorial staff))
Published online: ((will be filled in by the editorial staff))

REFERENCES

[1] S. H. Park, A. Roy, S. Beaupré, S. Cho, N. Coates, J. S. Moon, D. Moses, M. Leclerc, K. Lee, A. J. Heeger, *Nature Photon.* **2009**, *3*, 297–302.

[2] J. Hou, H.-Y. Chen, S. Zhang, R. I. Chen, Y. Yang, Y. Wu, G. Li, *J. Am. Chem. Soc.* **2009**, *131*, 15586–15587.

[3] Y. Liang, Z. Xu, J. Xia, S.-T. Tsai, Y. Wu, G. Li, C. Ray, L. Yu, *Adv. Mater.* **2010**, *22*, E135–E138.

[4] M. A. Green, K. Emery, Y. Hishikawa, W. Warta, E. D. Dunlop, *Prog. Photovolt: Res. Appl.* **2012**, *20*, 12–20.

[5] W. U. Huynh, J. J. Dittmer, A. P. Alivisatos, A. P. *Science* **2002**, *295*, 2425–2427.

[6] N. C. Greenham, X. Peng, A. P. Alivisatos, *Phys. Rev. B* **1996**, *54*, 17628–17637.

[7] K. M. Coakley, Y. Liu, M. D. McGehee, K. L. Frindell, G. D. Stucky, G. D. *Adv. Funct. Mater.* **2003**, *13*, 301–306.

[8] C. Y. Kuo, W. C. Tang, C. Gau, T. F. Guo, D. Z. Jeng, *Appl. Phys. Lett.* **2008**, *93*, 033307.

[9] D. C. Olson, S. E. Shaheen, R. T. Collins, D. S. Ginley, *J. Phys. Chem. C* **2007**, *111*, 16640–16645.

[10] R. Zhu, C.-Y. Jiang, S. Ramakrishna, *Adv. Mater.* **2009**, *21*, 994–1000.

[11] S. D. Oosterhout, M. M. Wienk, S. S. Van Bavel, R. Thiedmann, L. J. A. Koster, J. Gilot, V. Schmidt, R. A. J. Janssen, *Nature Mater.* **2009**, *8*, 818–824.

[12] S. S. Van Bavel, E. Sourty, G. De With, J. Loos, *Nano Lett.* **2009**, *9*, 507–513.

[13] O. Stenzel, L. J. A. Koster, R. Thiedmann, S. D. Oosterhout, R. A. J. Janssen, V. Schmidt, *Adv. Funct. Mater.* **2012**, *22*, 1236–1244.

[14] H. K. Kodali, B. Ganapathysubramanian, Modelling Simul. Mater. Sci. Eng. **2012**, *20*, 035015.

[15] P. K. Watkins, A. B. Walker, G. L. B. Verschoor, *Nano Lett.* **2005**, *5*, 1814–1818.

[16] R. G. E. Kimber, A. B. Walker, G. E. Schroder-Turk, D. J. Cleaver, *Phys. Chem. Chem. Phys.* **2010**, *12*, 844–851.

[17] C. Groves, R. G. E. Kimber, A. B. Walker, *J. Chem. Phys.* **2010**, *133*, 144110.

[18] J. D. Kotlarski, P. W. M. Blom, L. J. A. Koster, M. Lenes, L. H. Slooff, *J. Appl. Phys.* **2008**, *103*, 084502.

[19] L. J. A. Koster, W. J. Van Strien, W. J. E. Beek, P. W. M. Blom, *Adv. Funct. Mater.* **2007**, *17*, 1297–1302.

[20] P. Langevin, *Ann. Chim. Phys.* **1903**, *28*, 433–530.

[21] A. Einstein, *Ann. Phys. (Leipzig)* **1905**, *322*, 549–560.

[22] G. A. H. Wetzelaer, L. J. A. Koster, P. W. M. Blom, *Phys. Rev. Lett.* **2011,** *107*, 066605.

[23] S. Selberherr, *Analysis and Simulation of Semiconductor Devices*, Springer-Verlag, Wien, **1984**.

[24] P. Ramachandran, G. Varoquaux, *IEEE Comput. Sci. Eng.*, **2011**, *13*, 40–51.

[25] R. A. Marsh, C. Groves, N. C. Greenham, *J. Appl. Phys. Lett.* **2007**, *101*, 083509.

[26] C. Groves, R. A. Marsh, N. C. Greenham, *J. Chem. Phys.* **2008**, *129*, 114903.

[27] T. Offermans, S. C. J. Meskers, R. A. J. Janssen, *Chem. Phys.* **2005**, 308, 125–133.

[28] C. Groves, N. C. Greenham, *Phys. Rev. B* **2008**, *78*, 155205.

[29] C. Deibel, T. Strobel, V. Dyakonov, *Phys. Rev. Lett.* **2009**, *103*, 036402.

[30] P. Peumans, S. Uchida, S. R. Forrest, *Nature* **2003**, *425*, 158–162.

[31] J. E. Kroeze, T. J. Savenije, M. J. W. Vermeulen, J. M. Warman, *J. Phys. Chem. B* **2003**, *107*, 7696–7705.

[32] C. Goh, S. R. Scully, M. D. McGehee, *J. Appl. Phys.* **2007**, *101*, 114503.

[33] P. E. Shaw, A Ruseckas, I. D. W. Samuel, *Adv. Mater.* **2008**, *20*, 3516–3520.

[34] O. V. Mikhnenko, H. Azimi, M. Scharber, M. Morana, P. W. M. Blom, M. A. Loi, *Energy Environ. Sci.* **2012**, *5*, 6960–6965.

[35] More precisely, it is assumed that $D_X\tau = 25\ \mathrm{nm}^2$.

[36] S. D. Oosterhout, L. J. A. Koster, S. S. Van Bavel, J. Loos, O. Stenzel, R. Thiedmann, V. Schmidt, B. Campo, T. J. Cleij, L. Lutzen, D. Vanderzande, M. M. Wienk, R. A. J. Janssen, *Adv. Energy Mater.* **2011**, *1*, 90–96.

[37] V. D. Mihailetchi, H. X. Xie, B. De Boer, L. J. A. Koster, P. W. M. Blom, *Adv. Funct. Mater.* **2006**, *16*, 699–708.

[38] V. D. Mihailetchi, J. Wildeman, P. W. M. Blom, *Phys. Rev. Lett.* **2005**, *94*, 126602.

[39] A. Pivrikas, N. S. Sariciftci, G. Juška, R. Österbacka, *Prog. Photovolt: Res. Appl.* **2007**, *15*, 677–696.

[40] L. J. A. Koster, V. D. Mihailetchi, R. Ramaker, P. W. M. Blom, *Appl. Phys. Lett.* **2005**, *86*, 123509.

[41] O. Stenzel, H. Hassfeld, R. Thiedmann, L. J. A. Koster, S. D. Oosterhout, S. S. Van Bavel, M. M. Wienk, J. Loos, R. A. J. Janssen, V. Schmidt, *Ann. Appl. Stat.* **2011**, *5*, 1920–1947.

[42] B. Walker, C. Kim, T.-Q. Nguyen, *Chem. Mater.* **2011**, *23*, 470–482.

FIGURES

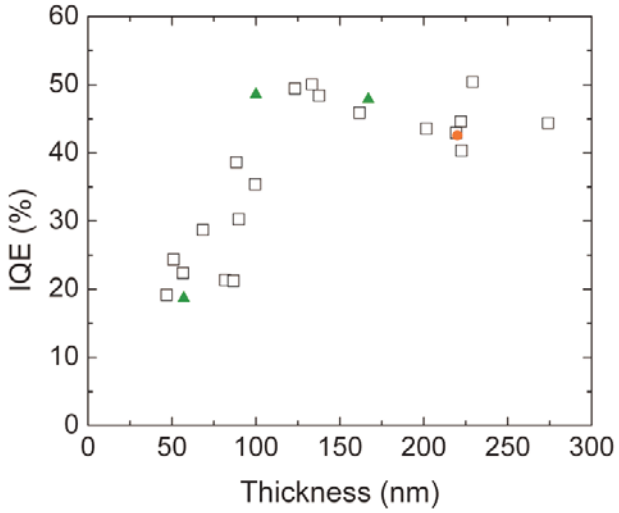

Figure 1. Internal quantum efficiency of P3HT/ZnO solar cells as a function of layer thickness. Open symbols represent the data from Oosterhout *et al.*[11] The simulation results for three thicknesses, where experimental 3D data were available, are denoted by the green triangles. The data point at 220 nm (red dot) is obtained by adding extra thickness to the 167-nm morphology data.

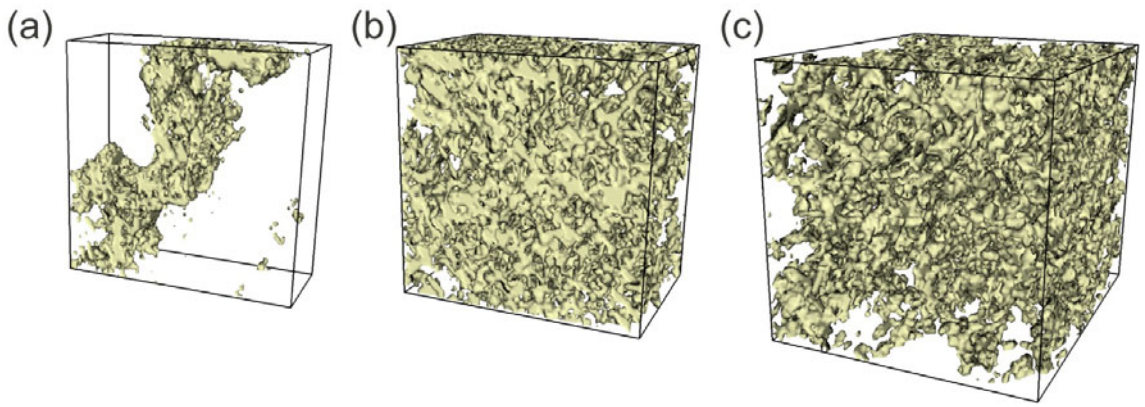

Figure 2. Reconstructed volumes of P3HT/ZnO layers of (a) 57 nm, (b) 100 nm, and (c) 167 nm thickness. P3HT appears transparent, ZnO gray. The lateral dimensions are 140 × 140 nm^2, which is a quarter of the total simulation volume. The front of the image corresponds to the anode.

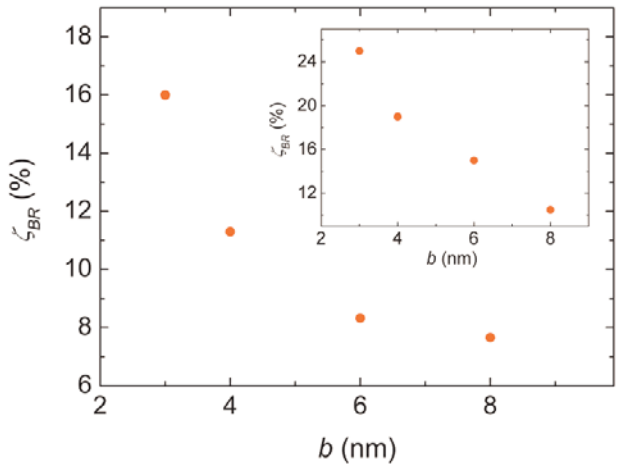

Figure 3. The bimolecular recombination loss ζ_{BR} as a function of the average feature size as calculated with the drift-diffusion model. The inset shows Monte-Carlo data re-plotted from Ref. 16.

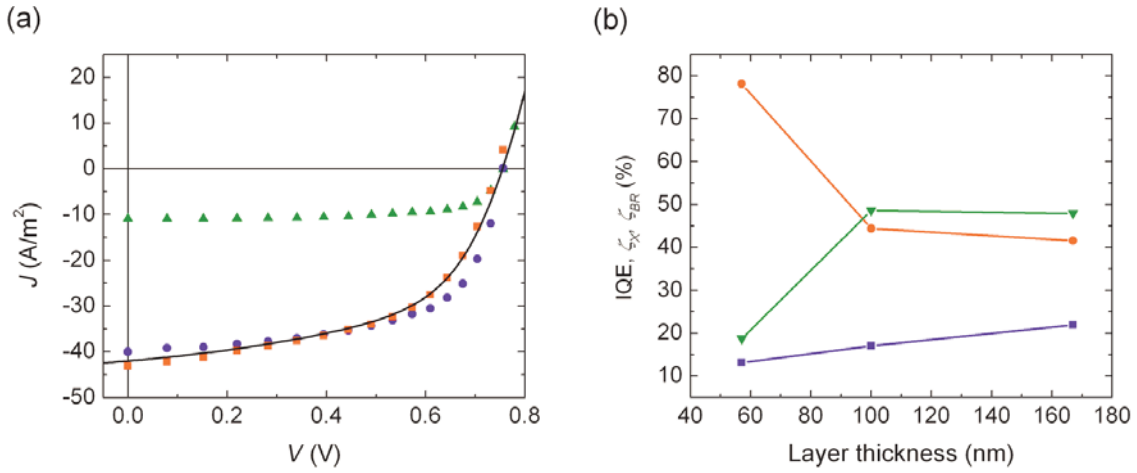

Figure 4. (a) Simulated current-voltage characteristics of the three different thicknesses ((green triangles) 57 nm, (blue dots) 100 nm, (red squares) 167 nm). For comparison, the experimental current-voltage curve of a 162-nm thick device is also included (line). (b) Internal quantum efficiency (green triangles), exciton loss ζ_X (red dots) and bimolecular recombination loss ζ_{BR} (blue squares). Lines are intended to guide the eye.

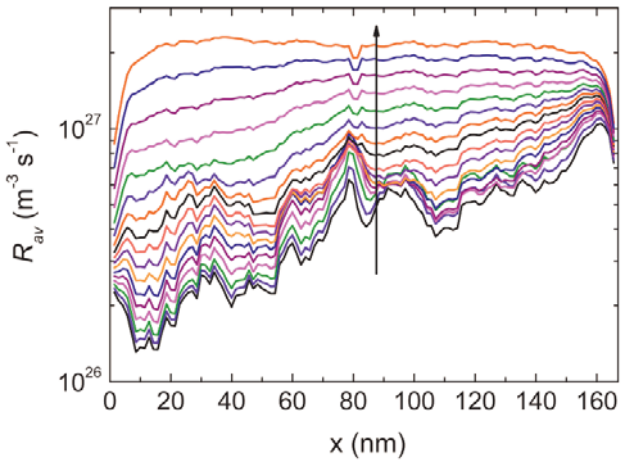

Figure 5. Average recombination rate R_{av} as a function of the distance x from the cathode in the 167 nm morphology. The arrow indicates increasing the applied voltage from short-circuit to open-circuit conditions.

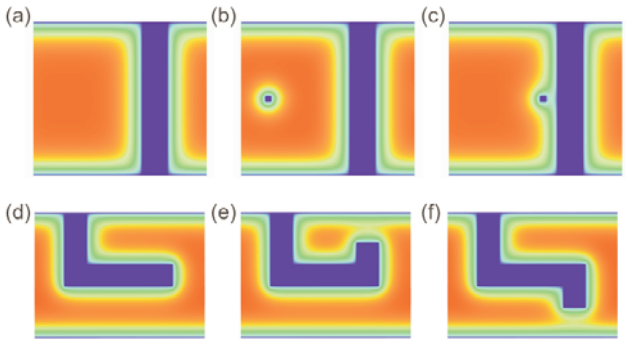

Figure 6. Exciton density (red = highest) on schematic morphologies. The plots show the exciton density perpendicular to the substrate with the cathode at the top of each graph and the anode at the bottom. The ZnO phase shows up as dark blue (zero exciton density). (a)-(c) The presence of isolated clusters of ZnO is only detrimental if the clusters are close to the main ZnO backbone: (a) and (b) have equal IQE, while in (c) the IQE is lower as the cluster "steals" excitons that would otherwise be harvested by the main ZnO backbone. (d)-(f) Cul-de-sacs in the morphology can reduce IQE. The current in (e) is reduced compared to (d) even though more excitons are harvested as the carriers are trapped in the cul-de-sac. The morphology in (f) harvests as many excitons as the one in (e), but also allows the photo-generated carriers to escape to the electrodes yielding a higher IQE.

Table 1. Parameters used to compare the drift-diffusion model with the Monte-Carlo data by Kimber *et al.*[16]

parameter	value	source
grid size	64×64×64	Ref. a
grid spacing	1 nm	Ref. a
μ_p	10^{-8} m^2/Vs	Ref. a
μ_n	10^{-8} m^2/Vs	Ref. a
ε_r	4	Ref. a
W_{cathode}	3.65 eV	Ref. b
W_{anode}	4.95 eV	Ref. a
HOMO donor	-5.1 eV	Ref. a
LUMO acceptor	-3.5 eV	Ref. a
exciton diffusion length	6 nm	Ref. a
absorbed photons[c]	2.5×10^{20} m^{-2} s^{-1}	Ref. a
N_{cv}	2.5×10^{25} m^{-3}	Ref. d

[a)]Ref. 16 and references therein; [b)]The electrode work functions are derived from the built-in voltage (1.3 V) and the energy levels of the materials used in Ref. 15; [c)]A Gaussian optical field profile was used.[15]; [d)] L. J. A. Koster, E. C. P. Smits, V. D. Mihailetchi, P. W. M. Blom, *Phys. Rev. B.* **2005**, *72*, 085205.

Table 2. Parameters used to fit the optoelectronic model to the IQE data in Figure 1.

parameter	value	source
lateral grid size	200×200	
grid spacing	1.4 nm[a]	
μ_p	4×10^{-8} m^2/Vs	Ref. b
μ_n	4×10^{-8} m^2/Vs	see text
ε_r	4[c]	
HOMO P3HT	-4.9 eV	Ref. d
electron affinity ZnO	-3.8 eV[e]	
W_{cathode}	3.8 eV[f]	
W_{anode}	4.9 eV[f]	
exciton diffusion length	5 nm	see text
N_{cv}	2.5×10^{25} m^{-3}	Ref. g
γ_{pre}	0.03	fit to IQE
absorbed photons 57 nm	3.6×10^{20} m^{-2} s^{-1}	experiment
absorbed photons 100 nm	5.1×10^{20} m^{-2} s^{-1}	experiment
absorbed photons 167 nm	5.6×10^{20} m^{-2} s^{-1}	experiment
absorbed photons 220 nm	6.6×10^{20} m^{-2} s^{-1}	experiment

[a)] Taken equal to typical hop lengths found in conjugated materials; [b)] Ref. 36; [c)] Taken as the average of the relative dielectric constants of ZnO (5) and conjugated polymers (3); [d)] J. Hou, T. L. Chen, S. Zhang, L. Huo, S. Sista, Y. Yang, *Macromolecules* **2009**, *42*, 9217–9219; [e)] The electron affinity of ZnO was obtained by fitting to the open-circuit voltage (~0.75 V for the best devices) of the illuminated P3HT/ZnO solar cells; [f)] The contacts were assumed to be ohmic and their work functions therefore equal to the respective energy levels of the materials. [g)] L. J. A. Koster, E. C. P. Smits, V. D. Mihailetchi, P. W. M. Blom, *Phys. Rev. B.* **2005**, *72*, 085205.

Table 3. The influence of removing isolated ZnO clusters and removing cul-de-sacs from the original 167-nm morphology on the exciton loss ζ_X, bimolecular recombination loss ζ_{BR} and the internal quantum efficiency.

	original	clusters removed	cul-de-sacs removed
ζ_X (%)	42	46	51
ζ_{BR} (%)	22	11	5
IQE (%)	48	48	47

The table of contents entry should be fifty to sixty words long (max. 400 characters):

The authors present a quantitative link between the internal quantum efficiency and morphology of polymer/ZnO solar cells. The morphologies of three active layers with different thicknesses were used as direct input for a 3D numerical device model. This first direct use of morphological data in a numerical model highlights the importance of morphology in solar cells.

Keywords: conjugated polymers; organic electronics; photovoltaic devices; solar cells; zinc oxide

L. Jan Anton Koster, Ole Stenzel, Stefan D. Oosterhout, Martijn M. Wienk, Volker Schmidt, and René A. J. Janssen*

Morphology and Efficiency: The case of polymer/ZnO solar cells

ToC figure (55 mm broad × 50 mm)

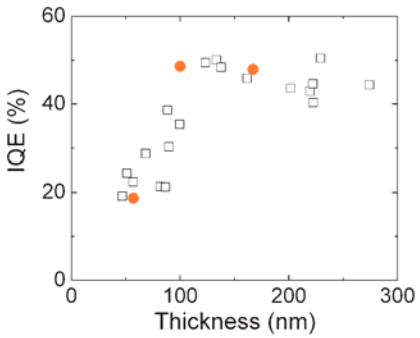

Supporting Information

for *Adv. Energy Mater.*, DOI: 10.1002/aenm.((please add manuscript number))

Morphology and Efficiency: The case of polymer/ZnO solar cells

L. Jan Anton Koster, Ole Stenzel, Stefan D. Oosterhout, Martijn M. Wienk, Volker Schmidt, and René A. J. Janssen*

Mirror procedure for obtaining extra thickness

The morphology consists of slices (or cross-sections) in the plane of the substrate. Due to experimental constraints the slices near the cathode and anode were difficult to binarize and contained artifacts. Instead of using these slices, we discarded these and added extra slices to obtain the right thickness. Suppose we have slices 1,...,N and wish to add M slices. This is accomplished by mirroring part of the morphology such that slice N+i is equal to slice N-i, where i=1,..,M. Figure S1 compares the current-voltage characteristics of an original morphology (all usable slices) with those of a partly mirrored morphology. Clearly, there is very little difference between these characteristics, which shows that the mirroring procedure does not induce any artifacts.

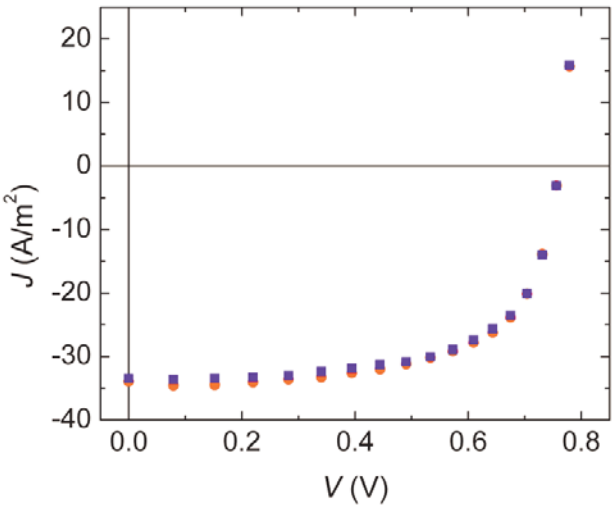

Figure S1. Influence of mirroring part of the morphology in order to obtain a larger thickness. This graph shows the current-voltage characteristics two morphologies of 67 nm thickness: The original morphology (red dots) is a stack of 67 nm thickness taken from the 100 nm sample, the mirrored one (blue squares) is obtained by taking only half of the stack and adding the other half by mirroring. The resulting current-voltage curves are virtually identical.